INTERNATIONAL JOURNAL FOR NUMERICAL METHODS IN FLUIDS, VOL. 23, 221–239 (1996)

FORCE FIELDS ON INVISCID, SLENDER, ANNULAR LIQUID JETS

J. I. RAMOS

Departamento de Lenguajes y Ciencias de la Computación, ETS Ingenieros Industriales, Universidad de Málaga, Plaza El Ejido, s/n, E-29013 Málaga, Spain

SUMMARY

Regular perturbation expansions are used to analyse the fluid dynamics of unsteady, inviscid, slender, thin, incompressible (constant density), axisymmetric, upward and downward, annular liquid jets subjected to non-homogeneous, conservative body forces when both the annular jets are very thin and the gases enclosed by and surrounding the jet are dynamically passive. Both inertia- and capillarity-dominated annular jets are considered. It is shown that, for inertia-dominated jets, closure of the leading-order equations is achieved at second order in the perturbation parameter, which is the slenderness ratio, whereas closure is achieved at first order for capillarity-dominated jets. The steady leading-order equations are solved numerically by means of both an adaptive finite difference method which maps the curvilinear geometry of the jet onto a unit square and a fourth-order-accurate Runge–Kutta technique. It is shown that the fluid dynamics of steady, annular liquid jets is very sensitive to the Froude and Weber numbers and nozzle exit angle in the presence of non-homogeneous, conservative body forces. For upward jets with inwardly or axially directed velocities at the nozzle exit the effect of the non-homogeneous, conservative body forces is to increase the leading-order axial velocity component, decrease the jet's mean radius and move the stagnation point downstream. For downward jets with radially outward velocity at the nozzle exit the axial velocity component decreases monotonically as the magnitude of the non-homogeneous, conservative body forces is increased.

KEY WORDS perturbation methods; annular liquid jets; non-homogeneous body forces; adaptive finite difference methods

1. INTRODUCTION

In a previous paper the author[1] analysed the fluid dynamics of slender, thin, upward and downward, annular liquid jets (Figure 1) subject to surface tension and gravity by means of regular perturbation methods using the velocity potential. In this paper the fluid dynamics of slender, thin, annular liquid jets subject to surface tension, gravity and non-homogeneous, conservative body forces which depend on the jet's thickness is analysed by means of perturbation methods using the Euler equations. The paper may be considered as complementary to Reference 1, where the fluid dynamics of slender, annular liquid jets was analysed in the absence of non-homogenous, conservative body forces. Therefore, by comparing the formulation and results presented here with those of Reference 1, one may easily determine the effects of non-homogeneous, conservative body forces on inviscid, slender, thin, annular jets.

The paper has been organized as follows. The dimensional governing equations and boundary conditions are presented in Section 2, together with the non-homogeneous, conservative body forces. Perturbation methods for inviscid, thin and slender, annular liquid jets are employed in Section 3 to

CCC 0271–2091/96/030221–19

Received May 1995
Revised November 1995

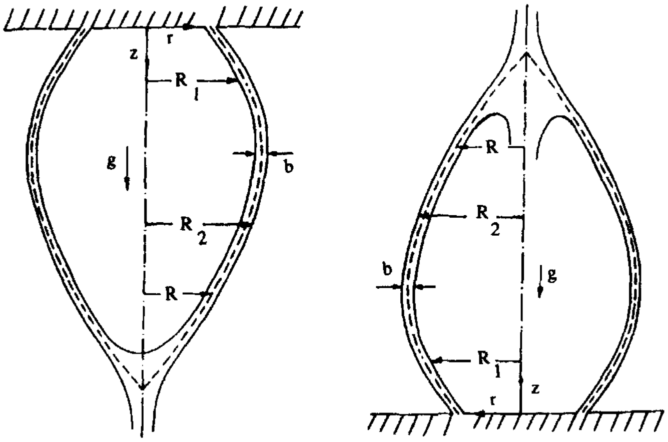

Figure 1. Schematic diagrams of downward (left) and upward (right) annular liquid jet

derive the leading-order equations of both inertia- and capillarity-dominated, annular jets when the non-homogeneous, conservative body forces are important at leading order. Steady, annular liquid jets are considered in Section 4, where the analysis presented in the paper is extended to other types of non-homogeneous, conservative body forces. In Section 5 some examples which illustrate the steady fluid dynamics of inertia- and capillarity-dominated, upward and downward, annular liquid jets are presented as functions of the nozzle exit angle, magnitude of the non-homogeneous, conservative body forces and Froude and Weber numbers.

2. GOVERNING EQUATIONS

The fluid dynamics of unsteady, axisymmetric, incompressible (constant density), inviscid, irrotational, annular liquid jets subjected to non-homogeneous, conservative body forces is governed by the continuity and Euler equations and the irrotationality condition, i.e.

$$\frac{\partial u^*}{\partial z^*}+\frac{1}{r^*}\frac{\partial(v^*r^*)}{\partial r^*}=0, \tag{1}$$

$$\rho^*\left(\frac{\partial u^*}{\partial t^*}+u^*\frac{\partial u^*}{\partial z^*}+v^*\frac{\partial u^*}{\partial r^*}\right)=-\frac{\partial p^*}{\partial z^*}+\rho^*g^*-\frac{\partial W^*}{\partial z^*}, \tag{2}$$

$$\rho^*\left(\frac{\partial v^*}{\partial t^*}+u^*\frac{\partial v^*}{\partial z^*}+v^*\frac{\partial v^*}{\partial r^*}\right)=-\frac{\partial p^*}{\partial r^*}-\frac{\partial W^*}{\partial r^*}, \tag{3}$$

$$\frac{\partial u^*}{\partial r^*}=\frac{\partial v^*}{\partial z^*}, \tag{4}$$

where asterisks denote dimensional quantities, r^* and z^* are the radial and axial co-ordinates respectively, p^* is the pressure, ρ^* is the density, g^* is the gravitational acceleration, W^* is the potential of non-homogeneous, conservative body forces and u^* and v^* denote the liquid's axial and radial velocity components respectively.

In this paper it is assumed that the potential of non-homogeneous, conservative body forces is

$$W^* = \frac{A^*}{b^{*3}}, \tag{5}$$

where A^* denotes a positive constant, here referred to as the constant of the non-homogeneous, conservative body forces or simply as the body force constant, and b^* is the annular jet's thickness.

Equation (5) has the same functional dependence on the annular jet's thickness as the force potential of intermolecular, attractive, long-range London–van der Waals forces which play an important role in very thin, viscous films and fluid layers.[2–4] For example, the break-up of slow viscous films along solid surfaces and slow viscous free films has been attributed to London–van der Waals forces.[4–6] These forces are due to the asymmetry of intermolecular force fields in the neighbourhood of phase boundaries.

According to equation (5), W^* is only a function of t^* and z^* and the non-homogeneous, conservative body forces have no component along the radial direction. Note that the jet's thickness has been measured perpendicularly to the z-axis; if it were measured perpendicularly to the jet's mean radius, b^* would have to be replaced by h^* in equation (5), where $h^* = b^* \cos\theta$, $\tan\theta = \partial R^*/\partial z^*$ and R^* denotes the jet's mean radius, i.e. $R^* = (R_1^* + R_2^*)/2$.

Equations (1)–(4) are subject to the following kinematic and dynamic boundary conditions at the annular liquid jet's interfaces:

$$v^*(R_i^*, z^*, t^*) = \frac{\partial R_i^*}{\partial t^*} + u^*(R_i^*, z^*, t^*)\frac{\partial R_i^*}{\partial z^*}, \quad i = 1, 2, \tag{6}$$

$$P_1^* - p^*(R_1^*, z^*, t^*) = \sigma^*\left(\frac{1}{R_1^*[1 + (\partial R_1^*/\partial z^*)^2]^{1/2}} - \frac{\partial^2 R_1^*/\partial z^{*2}}{[1 + (\partial R_1^*/\partial z^*)^2]^{3/2}}\right), \tag{7}$$

$$p^*(R_2^*, z^*, t^*) - P_2^* = \sigma^*\left(\frac{1}{R_2^*[1 + (\partial R_2^*/\partial z^*)^2]^{1/2}} - \frac{\partial^2 R_2^*/\partial z^{*2}}{[1 + (\partial R_2^*/\partial z^*)^2]^{3/2}}\right), \tag{8}$$

where R_1^* and R_2^* are the radii of the jet's inner and outer interfaces respectively, σ^* is the liquid's surface tension and P_1^* and P_2^* denote the pressures of the gases enclosed by and surrounding the annular liquid jet respectively. These gases will be assumed to be dynamically passive, i.e. P_1^* and P_2^* will be assumed to be spatially uniform, since their density and dynamic viscosity are in general much smaller than those of liquids.

In addition, initial conditions and boundary conditions at $z^* = 0$, i.e. at the nozzle exit, must be provided. These boundary conditions must be obtained by matching the inviscid flow inside the nozzle to that of the free, annular jet. Since the flow inside the nozzle must satisfy the no-penetration condition at the solid walls, whereas the boundary conditions for the free, annular jet involve free surfaces, a transition from the no-penetration to the free surface flow is expected. Such a transition is not considered in this paper, where the interest lies in the region below the nozzle exit.

For thin and long or slender, annular liquid jets, $\lambda = b_0^*/R_0^*$ and $\epsilon = R_0^*/L^* \ll 1$, where b_0^*, R_0^* and L^* denote respectively (constant) reference values for the jet's thickness and mean radius and a characteristic axial distance or wavelength; for example, they may denote the jet's mean thickness and radius at the nozzle exit and the convergence length respectively. In this paper it is assumed that $\lambda = O(\epsilon^2)$.

If the radial and axial co-ordinates are non-dimensionalized with respect to R_0^* and L^* respectively, the axial and radial velocity components with respect to u_0^* and ϵu_0^* respectively, where u_0^* denotes a characteristic axial velocity component, b^* with respect to R_0^*, t^* with respect to L^*/u_0^*, $R_i^* (i = 1, 2)$ with respect to R_0^* and the pressure with respect to $\rho^* u_0^{*2}$, where u_0^* is a (constant) reference axial velocity component at the nozzle exit, equations (1)–(4) and (6)–(8) become

$$\frac{\partial u}{\partial z} + \frac{1}{r}\frac{\partial (vr)}{\partial r} = 0, \tag{9}$$

$$\frac{\partial u}{\partial t} + u\frac{\partial u}{\partial z} + v\frac{\partial u}{\partial r} = -\frac{\partial p}{\partial z} + \frac{1}{Fr} + \frac{A_{\mathrm{H}}}{b^4}\frac{\partial b}{\partial z}, \tag{10}$$

$$\epsilon^2\left(\frac{\partial v}{\partial t} + u\frac{\partial v}{\partial z} + v\frac{\partial v}{\partial r}\right) = -\frac{\partial p}{\partial r}, \tag{11}$$

$$\frac{\partial u}{\partial r} = \epsilon^2\frac{\partial v}{\partial z}, \tag{12}$$

$$v(R_i, z, t) = \frac{\partial R_i}{\partial t} + u(R_i, z, t)\frac{\partial R_i}{\partial z}, \quad i = 1, 2, \tag{13}$$

$$P_1 - p(R_1, z, t) = \frac{1}{We}\left(\frac{1}{R_1[1 + \epsilon^2(\partial R_1/\partial z)^2]^{1/2}} - \frac{\epsilon^2 \partial^2 R_1/\partial z^2}{[1 + \epsilon^2 \partial R_1/\partial z^2]^{3/2}}\right), \tag{14}$$

$$p(R_2, z, t) - P_2 = \frac{1}{We}\left(\frac{1}{R_2[1 + \epsilon^2(\partial R_2/\partial z)^2]^{1/2}} - \frac{\epsilon^2 \partial^2 R_2/\partial z^2}{[1 + \epsilon^2(\partial R_2/\partial z)^2]^{3/2}}\right), \tag{15}$$

where $Fr = u_0^{*2}/g^* L^*$ is the Froude number, $We = \rho^* R_0^* u_0^{*2}/\sigma^*$ is the Weber number and $A_{\mathrm{H}} = 3A^*/\rho^* u_0^{*2} R_0^{*3}$ denotes the non-dimensional constant associated with the non-homogeneous, conservative body forces.

The length used to non-dimensionalize the axial co-ordinate in this section may be replaced by u_0^{*2}/g^*, which corresponds to a Froude number equal to one, and the condition of slenderness implies that $u_0^{*2}/g^* \gg R_0^*$.

Depending on the magnitude of the Froude and Weber numbers and the non-dimensional constant which characterizes the non-homogeneous, conservative body forces, several flow regimes may be identified. Note that the Weber and Froude numbers represent the ratios of inertia to gravity and surface tension respectively, while the non-dimensional body force constant is the ratio of non-homogeneous, conservative body forces to inertia. In the absence of non-homogeneous, conservative body forces, the inertia-dominated flow regime corresponding to large Weber numbers, i.e. $We = W\epsilon^{-2n}$ and $Fr = F\epsilon^{-2m}$, and the capillary regime corresponding to $We = O(1)$ and $Fr = F\epsilon^{-2m}$, where W and F are $O(1)$ and n and m are natural numbers such that $n \geqslant 1$ and $m \geqslant 0$, have been previously analysed[1] and will not be discussed here, where the emphasis will be placed on sufficiently thin, annular liquid jets such that the non-homogeneous, conservative body forces are important at leading order. We thereore assume that $A_{\mathrm{H}} = \epsilon^6 \bar{A}$, where $\bar{A} = O(1)$, and study an inertia- and a capillarity-dominated regime in Sections 2.1 and 2.2 respectively.

2.1. $We = O(\epsilon^{-4})$ and $Fr = O(1)$

If $We = \epsilon^{-4}W$, where $W = O(1)$ and $Fr = O(1)$, the liquid's velocity components, the pressure and the jet's mean radii at the inner and outer interfaces can be written in terms of ϵ^2 as

$$u = u_0 + \epsilon^2 u_2 + O(\epsilon^4), \tag{16}$$

$$v = v_0 + \epsilon^2 v_2 + O(\epsilon^4), \tag{17}$$

$$p = p_0 + \epsilon^2 p_2 + O(\epsilon^4), \tag{18}$$

$$R_1 = R_0 + \epsilon^2 R_{12} + O(\epsilon^4), \tag{19}$$

$$R_2 = R_0 + \epsilon^2 R_{22} + O(\epsilon^4). \tag{20}$$

Note that $b = R_2 - R_1 = \epsilon^2 b_2 + O(\epsilon^4)$, where, for example, $b_2 = R_{22} - R_{12}$.

Expansion of the kinematic (equation (13)) and dynamic (equations (14) and (15)) boundary conditions at R_1 and R_2 in Taylor series around R_0 followed by substitution of equations (16)–(20) into equations (9)–(15) results in a system of equations in powers of ϵ^2. Equating terms of $O(\epsilon^0)$ yields

$$\frac{\partial u_0}{\partial z} + \frac{1}{r}\frac{\partial(v_0 r)}{\partial r} = 0, \tag{21}$$

$$\frac{\partial u_0}{\partial t} + u_0\frac{\partial u_0}{\partial z} + v_0\frac{\partial u_0}{\partial r} = -\frac{\partial p_0}{\partial z} + \frac{1}{Fr} + \frac{\bar{A}}{b_2^4}\frac{\partial b_2}{\partial z}, \tag{22}$$

$$\frac{\partial p_0}{\partial r} = 0, \tag{23}$$

$$\frac{\partial u_0}{\partial r} = 0, \tag{24}$$

$$v_0(R_0, z, t) = \frac{\partial R_0}{\partial t} + u(R_0, z, t)\frac{\partial R_0}{\partial z}, \tag{25}$$

$$P_i - p_0(R_0, z, t) = 0, \quad i = 1, 2. \tag{26}$$

Equations (23) and (24) imply that $p_0 = C(z, t)$ and $u_0 = B(z, t)$ respectively, while equation (26) requires that, for mathematical compatibility, $p_0 = C(z, t) = P_1 = P_2$. Therefore, since the gases enclosed by and surrounding the annular liquid jet were assumed to be dynamically passive, p_0 is at most a function of time.

The solution of equation (21) is

$$v_0 = -\frac{B'}{2}r + \frac{D}{r}, \tag{27}$$

where D is a function of z and t and the prime denotes partial differentiation with respect to z.

Substitution of equation (27) into equation (25) yields

$$D = \frac{1}{2}\frac{\partial R_0^2}{\partial t} + \frac{1}{2}\frac{\partial(BR_0^2)}{\partial z}, \tag{28}$$

while equation (22) becomes

$$\frac{\partial B}{\partial t} + B\frac{\partial B}{\partial z} = \frac{1}{Fr} + \frac{\bar{A}}{b_2^4}\frac{\partial b_2}{\partial z}. \tag{29}$$

To $O(\epsilon^2)$ the radial momentum equation and dynamic boundary conditions become respectively

$$\frac{\partial p_2}{\partial r} = -\frac{\partial v_0}{\partial t} - u_0\frac{\partial v_0}{\partial z} - v_0\frac{\partial v_0}{\partial r}, \tag{30}$$

$$p_2(R_0, z, t) + R_{i2}\frac{\partial p_0(R_0, z, t)}{\partial r} = 0, \quad i = 1, 2. \tag{31}$$

The solution of equation (30) is

$$p_2 = -\left(\frac{\partial D}{\partial t} + BD'\right)\ln r - \frac{D^2}{2r^2} - \frac{r^2}{8}\left(B'^2 - 2BB'' - 2\frac{\partial B'}{\partial t}\right) + E(z, t), \tag{32}$$

where E can be calculated from the condition that (see equation (31)) $p_2(R_0, z, t) = 0$, i.e.

$$E(z, t) = \left(\frac{\partial D}{\partial t} + BD'\right)\ln R_0 + \frac{D^2}{2R_0^2} + \frac{R_0^2}{8}\left(B'^2 - 2BB'' - 2\frac{\partial B'}{\partial t}\right). \tag{33}$$

The kinematic boundary conditions to $O(\epsilon^2)$ are

$$R_{i2}\frac{\partial v_0}{\partial r} + v_2 = \frac{\partial R_{i2}}{\partial t} + u_0\frac{\partial R_{i2}}{\partial z} + R_{i2}\frac{\partial u_0}{\partial r} + u_2, \quad i = 1, 2, \tag{34}$$

which can be subtracted to yield

$$\frac{\partial(b_2R_0)}{\partial t} + \frac{\partial(b_2R_0B)}{\partial z} = 0, \tag{35}$$

which is the leading-order continuity equation.

The dynamic boundary conditions to $O(\epsilon^4)$ become

$$-\frac{\partial p_0}{\partial r}R_{14} - \frac{1}{2}\frac{\partial^2 p_0}{\partial r_2}R_{12}^2 - \frac{\partial p_2}{\partial r}R_{12} - p_4 = \frac{1}{WR_0}, \tag{36}$$

$$\frac{\partial p_0}{\partial r}R_{24} + \frac{1}{2}\frac{\partial^2 p_0}{\partial r^2}R_{22}^2 + \frac{\partial p_2}{\partial r}R_{22} + p_4 = \frac{1}{WR_0}. \tag{37}$$

Equations (36) and (37) may be added to yield

$$\frac{\partial p_2}{\partial r}b_2 = \frac{2}{WR_0}, \tag{38}$$

which may be written using equation (32) as

$$\frac{1}{R_0}\left(\frac{\partial D}{\partial t} + B\frac{\partial D}{\partial z}\right) + \frac{R_0}{4}\left[\left(\frac{\partial B}{\partial z}\right)^2 - 2\frac{\partial}{\partial z}\left(\frac{\partial B}{\partial t}\right) - 2B\frac{\partial^2 B}{\partial z^2}\right] = \frac{D^2}{R_0^3} + \frac{2}{WR_0b^2}. \tag{39}$$

Equation (39) may be further simplified by substituting $\partial B/\partial t$ from equation (29) into that equation.

Equations (28), (29), (35) and (39) represent a system of partial differential equations for B, D, R_0 and b_2 which has the same form as that for inviscid, annular liquid jets in the absence of non-homogeneous, conservative body forces;[1] therefore it may be analysed by means of the adaptive finite difference method developed in Reference 7. Once the values of B, D, R_0 and b_2 have been determined, E may be calculated from equation (33).

It must be pointed out that since equation (39) involves $\partial D/\partial z$, while equation (28) involves $\partial R_0/\partial z$, second-order spatial derivatives of R_0 with respect to z appear in equation (39). These derivatives demand that $B(0, t)$, $R_{10}(0, t)$, $R_{20}(0, t)$ and $\partial R_0(0, t)/\partial z$ be specified.

The equations derived so far are also valid for $We = O(\epsilon^{-n})$ with $n \geqslant 6$; for these Weber numbers W has to be set to infinity in equation (39). For $n = 2$ it can be easily shown that an inconsistency arises in the dynamic boundary conditions at $O(\epsilon^2)$.

The analysis presented in this subsection also holds for $Fr = O(\epsilon^{-2m})$, where m is a natural number greater than or equal to zero. The case $n = 0$ has been treated above, whereas the cases corresponding to $n \geqslant 1$ may be easily deduced from equation (29) by simply setting Fr to infinity in that equation. Furthermore, the regular perturbation method employed in this subsection indicates that, if the Weber number is sufficiently large, compatibility of the dynamic boundary conditions at the jet's interfaces implies that the liquid's pressure be identical to those of the gases enclosed by and surrounding the annular liquid jet.

In order to handle a pressure difference between the gases enclosed by and surrounding the annular jet, surface tension effects must be much larger than those considered in this subsection, as indicated in the next subsection.

2.2. $We = O(1)$ *and* $Fr = O(1)$

The capillarity-dominated flow regime is characterized by $We = O(1)$ and $Fr = F\epsilon^{-2m}$, where $F = O(1)$ and $m \geqslant 0$, and may be analysed in exactly the same manner as the inertia-dominated flow regime. Here, only the case $We = O(1)$ and $Fr = O(1)$, i.e. $m = 0$, is considered. For these values of the Weber and Froude numbers, equations (28), (29) and (35) hold, while the dynamic boundary conditions to $O(\epsilon^0)$ become

$$P_1 - p_0(R_0, z, t) = \frac{1}{WeR_0}, \qquad P_2 - p_0(R_0, z, t) = -\frac{1}{WeR_0}, \tag{40}$$

which may be added and subtracted to yield respectively

$$p_0 = \frac{P_1 + P_2}{2}, \qquad P_1 - P_2 = \frac{2}{WeR_0}, \tag{41a, b}$$

i.e. the difference between the pressure of the gases enclosed by and that of the gases surrounding the annular liquid jet is balanced by surface tension. Furthermore, since these gases were assumed to be dynamically passive, equations (41a) and (41b) imply that both the liquid's pressure and the jet's mean radius respectively are at most functions of time, i.e. the annular liquid jet is a cylindrical one. Equation (41b) may be used to determine R_0 and equations (29) and (35) may be employed to determine B and b_2.

The analysis presented in this subsection is also valid for $Fr = O(\epsilon^{-2m})$, where m is a natural number greater than or equal to zero. The case $n = 0$ has been treated above, whereas the cases $n \geqslant 1$ may be easily deduced from equation (29) by simply setting Fr to infinity in that equation. Furthermore, the results presented in this and the previous subsection reduce to those of Reference 1 in the absence of non-homogeneous, conservative body forces.

It must be noted that the perturbation methods of this subsection indicate that, when the Weber number is $O(1)$, the leading-order equations are closed at leading order, while the results of the previous subsection indicate that, for large Weber numbers, closure of the leading-order equations is achieved at fourth-order in the dynamic boundary conditions at the jet's interfaces.

3. STEADY, ANNULAR LIQUID JETS

The equations presented in Sections 2.1 and 2.2 have analytical solutions for steady, annular liquid jets as indicated in the next subsection.

3.1. *Inertia-dominated, annular liquid jets*

For steady, inertia-dominated jets the solutions of equations (35) and (29) are respectively

$$BR_0b_2 = \alpha, \tag{42}$$

$$B = \left(1 + \frac{2z}{G} + 2\beta - \frac{2\overline{A}}{3b_2^3}\right)^{1/2}, \tag{43}$$

where α is a (constant) non-dimensional volumetric flow rate and β is an integration constant. Without loss of generality α may be set equal to one. Furthermore, if equation (43) is assumed to be valid up to the nozzle exit, then $\beta = \overline{A}/3$, since $B(0)$, $R_0(0)$ and $b_2(0)$ may be set equal to one without loss of generality. Note that if $\overline{A} = 0$, equation (43) is the famous Torricelli free fall formula. Note also that the results presented in Sections 2.1 and 2.2 correspond to $G = Fr$.

For steady flows, equations (28) and (39) may be written, after rather tedious algebraic manipulations, as

$$\psi' = D, \tag{44}$$

$$\psi'' = \frac{D^2B^2 - \psi^2(\mathrm{d}B/\mathrm{d}z)^2 - 2\psi^2B\delta - (4\psi B/We)(2\psi B)^{1/2}}{2B\psi(B + \gamma\psi)}, \tag{45}$$

where

$$\begin{aligned}\delta = {} & \frac{2^{1/2}\overline{A}}{B + \overline{A}(2\psi^3B)^{1/2}}\left[\frac{D^2}{2}\left(\frac{B^3}{\psi}\right)^{1/2} + \frac{3D}{2}\frac{\mathrm{d}B}{\mathrm{d}z}(B\psi)^{1/2}\right] \\ & + \frac{1/G - \overline{A}D(2\psi B^3)^{1/2}}{[B + \overline{A}(2\psi^3B)^{1/2}]^2}\left\{\frac{\mathrm{d}B}{\mathrm{d}z}\left[1 + \overline{A}\left(\frac{\psi^3}{2B}\right)^{1/2}\right] + 3D\overline{A}\left(\frac{B\psi}{2}\right)^{1/2}\right\},\end{aligned} \tag{46}$$

$$\gamma = \frac{\overline{A}(2\psi B^3)^{1/2}}{B + \overline{A}(2\psi^3B)^{1/2}}, \tag*{47)}$$

$$\frac{\mathrm{d}B}{\mathrm{d}z} = \frac{1/G - \overline{A}D(2\psi B^3)^{1/2}}{B + \overline{A}(2\psi^3B)^{1/2}}, \tag{48}$$

$$R_0 = \left(\frac{2\psi}{B}\right)^{1/2}, \tag{49}$$

and $(G, H) = (Fr, W)$ for the analysis presented in Section 2.1. Annular liquid jets in microgravity correspond to $G = \infty$.

Equations (44)–(49) indicate that the values of R_{10}, R_{20} and R'_{10} or R'_{20} must be specified at the nozzle exit, i.e. at $z = 0$. Alternatively, one may specify R_0, R'_0 and $b_2(0)$ at the nozzle exit. For $R'_0 = \tan\theta_0$ and $B(0) = R_0(0) = b_2(0) = 1$ it may be easily shown from equations (49), (48) and (44) that

$$\psi(0) = \tfrac{1}{2}, \qquad \frac{\mathrm{d}B(0)}{\mathrm{d}z} = \frac{1}{1+\bar{A}}\left(\frac{1}{G} - \bar{A}\tan\theta_0\right), \tag{50}$$

$$D(0) = \frac{1}{2(1+\bar{A})}\left(\frac{1}{G} + (2+\bar{A})\tan\theta_0\right). \tag{51}$$

It must be pointed out that equations (44)–(51) reduce to those of Reference 1 when there are no non-homogeneous, conservative body forces, i.e. when $\bar{A} = 0$.

3.2. *Capillarity-dominated, annular liquid jets*

The steady state solutions of equations (29), (35) and (41) are

$$R_0 = \frac{We}{2}(P_1 - P_2), \qquad b_2 = \frac{1}{BR_0}, \tag{52}$$

$$B = \left[1 + \frac{2z}{G} + \frac{2\bar{A}}{3}\left(1 - \frac{1}{b_2^3}\right)\right]^{1/2} = \left(1 + \frac{2z}{G} + \frac{2\bar{A}}{3}(1 - B^3R_0^3)\right)^{1/2}, \tag{53}$$

where $G = Fr$ for the analysis presented in Section 2.2.

Equation (53) is a non-linear algebraic one which may be solved iteratively at each axial location by means of, for example, the secant method to determine B.

3.3. *Invariants of the leading-order equations*

For steady, annular liquid jets, equation (29) may be integrated analytically to yield

$$\tfrac{1}{2}B^2 - \frac{z}{G} + \frac{\bar{A}}{3b_2^3} = M, \tag{54}$$

where M is a constant that may be determined from the conditions at the nozzle exit.

Equation (54) corresponds to Torricelli's free fall formula and accounts for the non-homogeneous, conservative body forces acting on the annular liquid jet.

3.4. *Remarks*

The velocity u_0^* used in the non-dimensionalization was left unspecified in Sections 2 and 3. For inertia-dominated, annular liquid jets, i.e. when inertia is larger than surface tension, this velocity may be taken to be a constant reference velocity at the nozzle exit and the Froude and Weber numbers used in the text have their conventional meanings. For capillary, annular liquid jets, surface tension is larger than inertia effects and the reference velocity may be taken as $u_0^* = (\sigma^*/\rho^* R_0^*)^{1/2}$, so that $We = 1$ and $Fr = 1/\epsilon Bo$, where $Bo = \rho^* g^* R_0^{*2}/\sigma^*$ is the Bond number. Note that the Foude number used throughout the text could also be written as $Fr = \bar{F}/\epsilon$, where $\bar{F} = u_0^{*2}/g^* R_0^{*2}$ is a Froude number based on the jet's mean radius at the nozzle exit. In this case the analysis presented in Section 2 corresponds to $\bar{F} = O(\epsilon)$.

The analysis presented in Sections 2 and 3 also holds when b^* is replaced by $h^* = b^* \cos\theta$ (see equation (5)), where $\tan\theta = \partial R/\partial z$, i.e. when the thickness of the jet is measured perpendicularly to the jet's mean radius rather than perpendicularly to the symmetry axis, because it may be easily shown using equations (19) and (20) and $R = (R_1 + R_2)/2$ that $h = h^*/R_0^* = \epsilon^2 b_2 + O(\epsilon^4)$.

If the potential of non-homogeneous, conservative body forces is

$$S^* = \frac{A^*}{b^{*m}}, \tag{55}$$

where m is a natural number, the perturbation methods employed in this paper may also be used to analyze the fluid dynamics of inviscid, slender, thin, annular liquid jets subject to equation (55) if the non-homogeneous, conservative body forces are important at leading order as follows. For example, if $A_{\rm H} = \epsilon^{2m}\bar{A}$, where $\bar{A} = O(1)$ and $A_{\rm H} = mA^*/\rho^* u_0^{*2} R_0^{*m}$, equations (28), (35), (39) and (29) still hold provided that b_2^4 is replaced by b_2^{m+1} in these equations.

Finally, it must be emphasized that the formulation presented in this paper is a long-wave approximation which is not strictly valid at the nozzle exit and near the convergence point where the annular liquid jet merges onto the symmetry axis to become a solid one, because it does not account for the effects of the solid walls at $z = 0$ and the fact that the jet is not sufficiently thin at the convergence point. Despite this, the model has been applied from the nozzle exit to the convergence point.

4. PRESENTATION OF RESULTS

The leading-order equations derived in Sections 2 and 3 have been used to analyse the fluid dynamics of steady, long or slender, annular liquid jets subject to non-homogeneous, conservative body forces by means of an adaptive finite difference method similar to the one developed by Ramos.[7] This method maps the curvilinear geometry of the jet into a unit square and the equations in the transformed domain are solved by means of finite difference methods. The steady state results obtained with the adaptive technique were in remarkably good agreement with the solution of the equations presented in Section 3.1, which were solved by means of a fourth-order-accurate Runge–Kutta method. In fact, the local errors defined by

$$E_{\rm local}(z) = \tfrac{1}{2}B^2 - \frac{z}{G} + \frac{\bar{A}}{3b_2^3} - M \tag{56}$$

were found to be about 10^{-3} and 10^{-13} for the adaptive finite difference technique of Reference 7 and the Runge–Kutta method respectively for a step size $\Delta z = 0{\cdot}01$. The global errors defined by

$$E_{\rm global} = \sum_{i=1}^{NP} |E_{\rm local}(z_i)|, \tag{57}$$

where NP denotes the number of grid points in z, were found to increase as the annular liquid jet's convergence length increased.

The fact that the adaptive method yields larger errors than the Runge–Kutta technique is to be expected because of the higher accuracy of the latter and the fact that the adaptive method employs conservative, upwind finite differences for the convection terms which ensure conservation of linear momentum but do not conserve mechanical energy. In any case the differences in both the shapes and invariants of annular liquid jets were found to be so small that only the results obtained with the Runge–Kutta technique are reported in this section.

Some sample results illustrating the leading-order shapes of steady, upward and downward, annular liquid jets are presented in the next two subsections. These results correspond to $B(0) = R_0(0) = b_2(0) = 1$ and $\Delta z = 0{\cdot}001$.

4.1. *Steady, upward, annular liquid jets*

For upward, annular liquid jets the gravitational acceleration has the opposite direction to that of the axial velocity component of the liquid at the nozzle exit. Upward, annular liquid jets may be analysed by means of the equations presented in this paper by using a negative gravitational acceleration, i.e. a negative Froude number.

Figure 2 shows the annular jet's leading-order axial velocity component, mean radius and thickness as functions of the vertical co-ordinate z for $We = 100, Fr = -1$, three different values of the non-dimensional body force contant $\bar{A}$ and $dR_0(0)/dz = -0{\cdot}25$, 0 and $0{\cdot}25$. The results presented in the top and middle rows of Figure 2 indicate that the effect of the non-homogenous, conservative body force is to increase the leading-order axial velocity and decrease the leading-order mean radius for inwardly and axially directed flows at the nozzle exit and that the axial location at which the axial velocity component of upward, annular liquid jets becomes zero is not a monotonic function of the non-dimensional body force constant and nozzle exit angle. In fact, the results presented in the first and

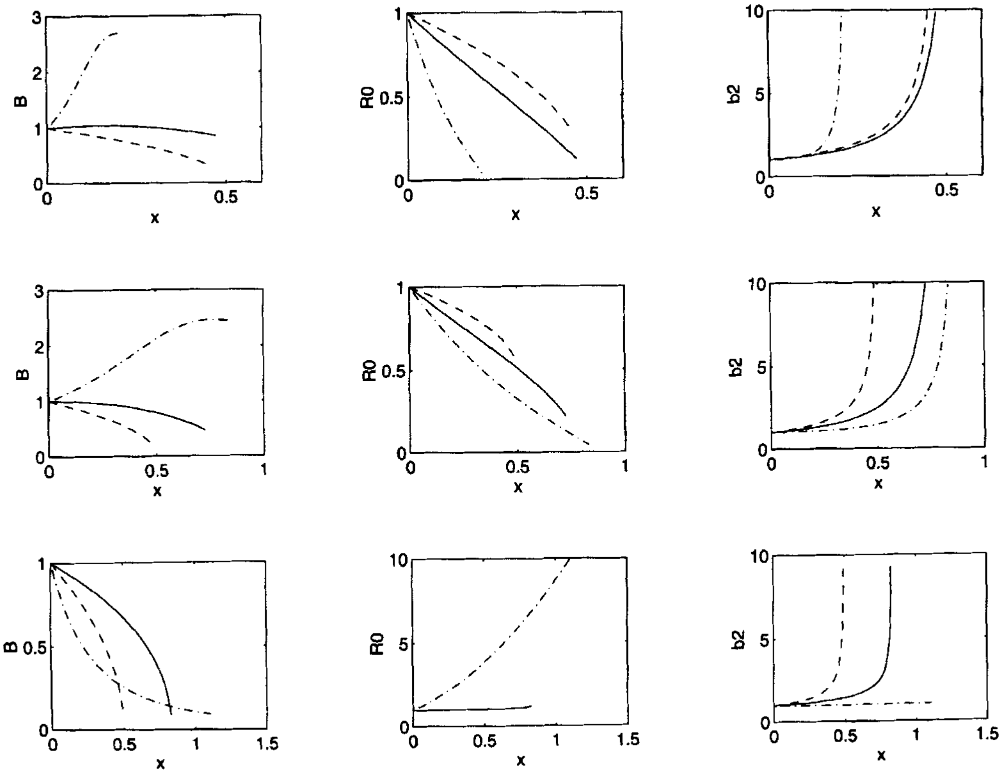

Figure 2. Leading-order axial velocity component (left column), mean radius (middle column) and thickness (right column) for inertia-dominated, upward, annular liquid jets. Top row: $dR_0(0)/dz = -0{\cdot}25$; middle row: $dR_0(0)/dz = 0$; bottom row: $dR_0(0)/dz = 0{\cdot}25$; $We = 100, Fr = -1, \bar{A} = 1$ (full lines), $\bar{A} = 0$ (broken lines), $\bar{A} = 10$ (chain lines)

second rows of Figure 2 for $\bar{A} = 1$ indicate that the stagnation point occurs further downstream than that for $\bar{A} = 0$; however, the stagnation point moves upstream as the non-dimensional body force constant is increased.

For axially directed flows at the nozzle exit the results illustrated in Figure 2 indicate that the location of the stagnation point moves downstream as $\bar{A}$ is increased; similar trends are observed for outwardly directed flows at the nozzle exit as indicated in the third row of Figure 2. This row also shows that the jet's thickness and mean radius are weak functions of the vertical co-ordinate for $\bar{A} = 1$ and 10 respectively. Furthermore, the slope of the jet's mean radius increases as the non-dimensional body force constant is increased. The third row of Figure 2 also illustrates that the concavity of the axial velocity component is downwards for $\bar{A} \leqslant 1$ and upwards otherwise.

It must be noted that in the absence of non-homogeneous, conservative body forces the stagnation point occurs at an axial location equal to $-Fr/2$ for $dR_0(0)/dz = 0$ (see equation (43)) as clearly shown in Figure 2. This axial location is nearly independent of the nozzle exit angle for $\bar{A} = 0$ and is smaller than that for $\bar{A} \neq 0$.

The results presented in Figure 2 also indicate that the axial velocity component is very sensitive to the nozzle exit angle for $\bar{A} > 1$ and is larger than that at the nozzle exit for $\bar{A} = 10$ and inwardly or axially directed flows at the nozzle exit.

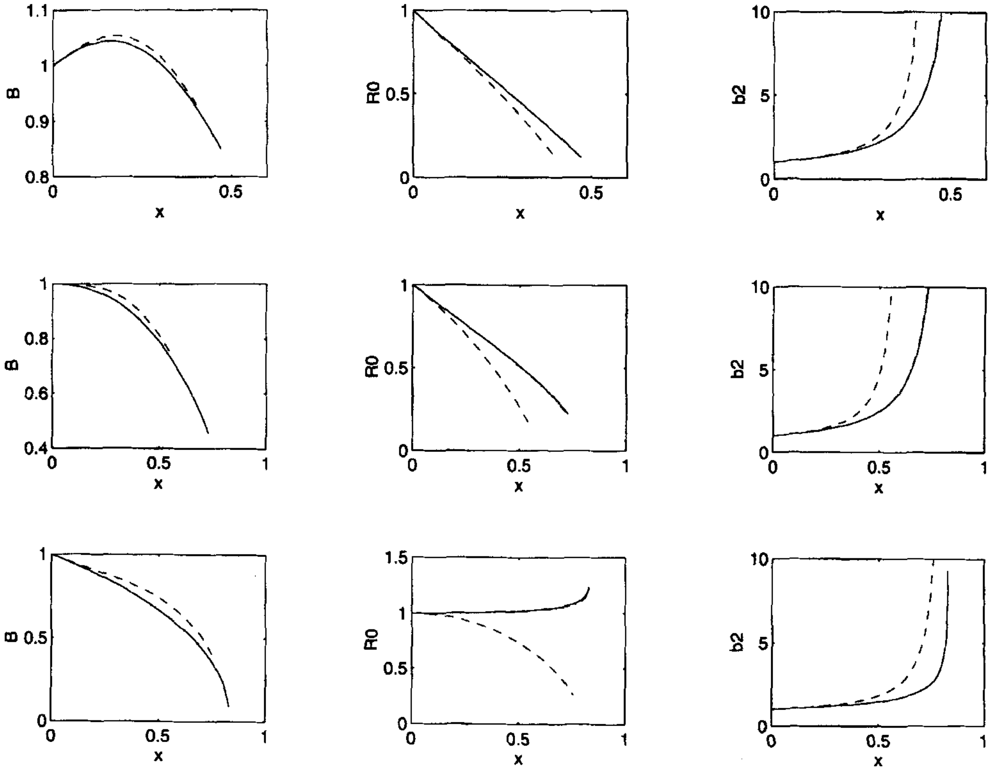

Figure 3. Leading-order axial velocity component (left column), mean radius (middle column) and thickness (right column) for inertia-dominated, upward, annular liquid jets. Top row: $dR_0(0)/dz = -0{\cdot}25$; middle row: $dR_0(0)/dz = 0$; bottom row: $dR_0(0)/dz = 0{\cdot}25$; $\bar{A} = 1$, $Fr = -1$, $We = \infty$ (full lines), $We = 1$ (broken lines), $We = 100$ (chain lines)

Figure 3 illustrates the effects of the Weber number and nozzle exit angle on the leading-order axial velocity component, mean radius and thickness of upward, annular liquid jets subject to non-homogeneous, conservative body forces. The results shown in this figure indicate that the shape of annular liquid jets is nearly independent of the Weber number for $We \geqslant 100$, the mean radius decreases and the axial velocity component increases as the Weber number is increased; the location of the stagnation point also increases as the Weber number is increased. It must be noted that for the values of the parameters considered in Figure 3 the axial velocity component first increases and then decreases for inwardly directed flows at the nozzle exit and decreases monotonically for axially or outwardly directed flows; the jet's thickness is a monotically increasing function of the axial coordinate regardless of the flow direction at the nozzle exit, whereas the jet's mean radius decreases and increases for inwardly or axially and outwardly directed flows respectively at the nozzle exit.

In Figure 4 the effects of the Froude number on the mean radius, thickness and axial velocity component of upward, annular liquid jets are shown as functions of the nozzle exit angle. Before discussing this figure, it is convenient to remark that in the absence of both gravity and non-homogeneous, conservative body forces the analysis presented in this paper indicates that the leading-order axial velocity is equal to one (see equation (43)).

Figure 4 indicates that the shape of annular liquid jets is nearly independent of the Froude number for $Fr \leqslant -1000$. For inwardly and axially directed flows at the nozzle exit the jet's mean radius increases and its thickness decreases as the Froude number is increased in absolute value; for

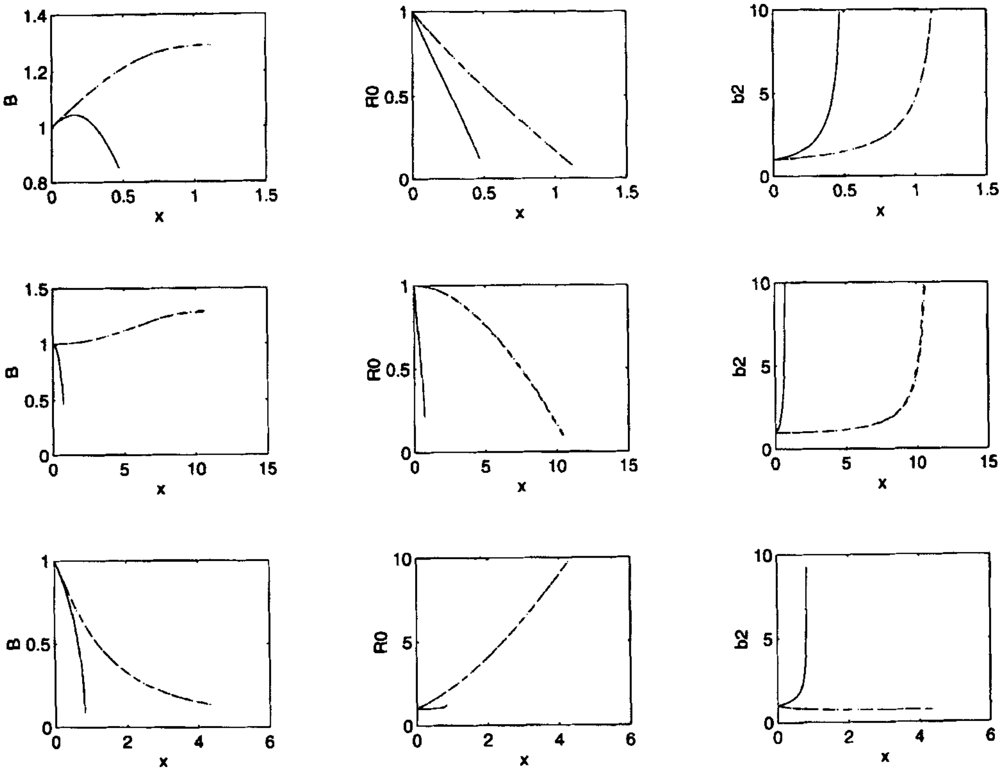

Figure 4. Leading-order axial velocity component (left column), mean radius (middle column) and thickness (right column) for inertia-dominated, upward, annular liquid jets. Top row: $\mathrm{d}R_0(0)/\mathrm{d}z = -0{\cdot}25$; middle row: $\mathrm{d}R_0(0)/\mathrm{d}z = 0$; bottom row: $\mathrm{d}R_0(0)/\mathrm{d}z = 0{\cdot}25$; $We = 100, \bar{A} = 1, Fr = -1$ (full lines), $Fr = -1000$ (broken lines), $Fr = -\infty$ (chain lines)

outwardly directed flows, however, the mean radius increases substantially as the Froude number is increased. Figure 4 also shows that the jet's axial velocity component is not a monotonic function of the nozzle exit angle. In fact, this velocity increases and decreases monotonically as a function of the axial co-ordinate for inward and outward flows respectively at the nozzle exit for $Fr \leqslant -1000$. For these Froude numbers and axially directed flows at the nozzle exit the axial velocity component exhibits an inflection point.

The results shown in Figure 4 clearly indicate that the effect of the non-homogeneous conservative body forces is to move the stagnation point downstream from the nozzle as the Froude number is increased in absolute value. Figure 4 also shows that for $Fr = -1$ the axial velocity component first increases and then decreases as a function of z.

The results presented in Figures 2–4 were obtained from the numerical solution of the equations presented in Section 3.1; therefore they correspond to inertia-dominated, upward, annular liquid jets. The mean radius, thickness and axial velocity component of capillary, upward, annular liquid jets are shown in Figure 5 as functions of the Froude number and non-dimensional body force constant. This figure corresponds to $B(0) = b_2(0) = 1$. Note that, since these jets preserve a cylindrical shape, their radii are not illustrated.

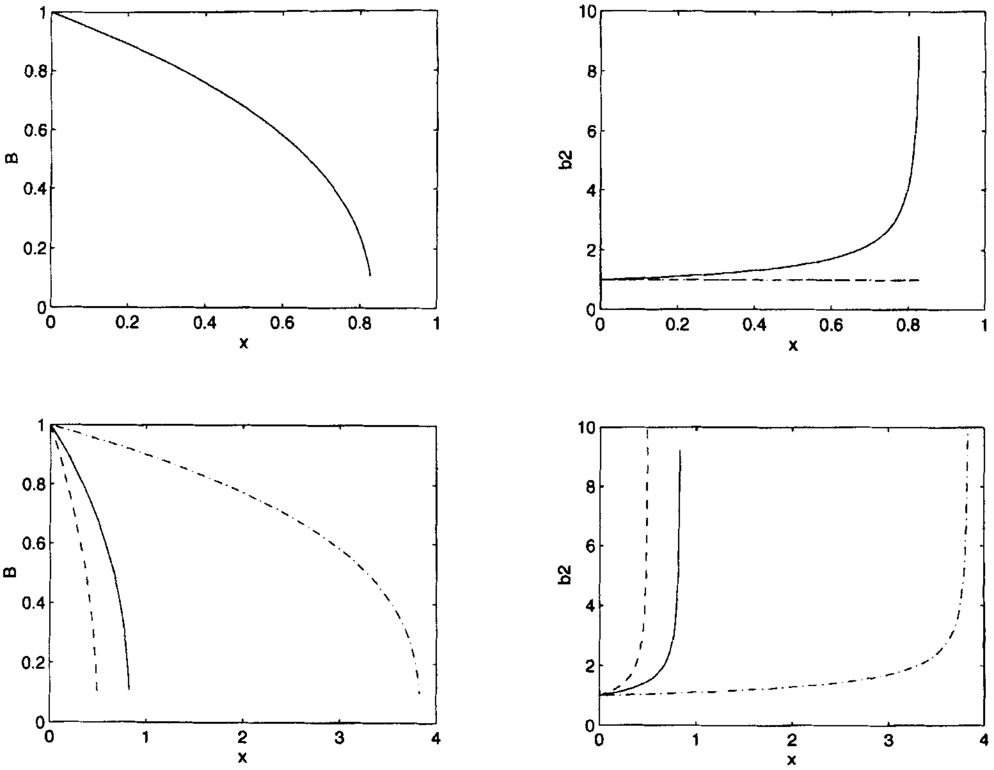

Figure 5. Leading-order axial velocity component (left column) and thickness (right column) for capillary, upward, annular liquid jets. Top row: $\bar{A} = 1, Fr = -1$ (full lines), Fr $= -1000$ (broken lines), Fr $= -\infty$ (chain lines); bottom row: $Fr = -1, \bar{A} = 1$ (full lines), $\bar{A} = 0$ (broken lines), $\bar{A} = 10$ (chain lines)

The first row of Figure 5 indicates that the axial velocity is a decreasing function of z and decays very little for $Fr \leqslant -1000$, while the second row shows that the axial location of the stagnation point is a monotonically increasing function of the non-homogeneous, conservative body forces, i.e. this point moves downstream as the non-dimensional body force constant is increased.

4.2. *Steady, downward, annular liquid jets*

In Figure 6 the effects of the non-dimensional body force constant and nozzle exit angle on the axial velocity component, mean radius and thickness of inertia-dominated, downward, annular liquid jets are illustrated. For inward flows at the nozzle exit both the mean radius and thickness are weak functions of the axial co-ordinate for $\bar{A} = 0$ and 1, while the velocity increases substantially as the non-dimensional body force constant is increased. Note that the axial velocity is not a monotonic function of $\bar{A}$, since it is higher in the absence of non-homogeneous, conservative body forces than for $\bar{A} = 1$.

For axially directed flows at the nozzle exit the second row of Figure 6 shows that the jet's mean radius increases and its thickness decreases as a function of z; both the mean radius and thickness are monotically increasing functions of $\bar{A}$. The axial velocity component is a monotonically increasing function of z in the absence of non-homogeneous, conservative body forces and decreases monotonically as $\bar{A}$ is increased. Note that for the flows considered here the non-homogenous, conservative body

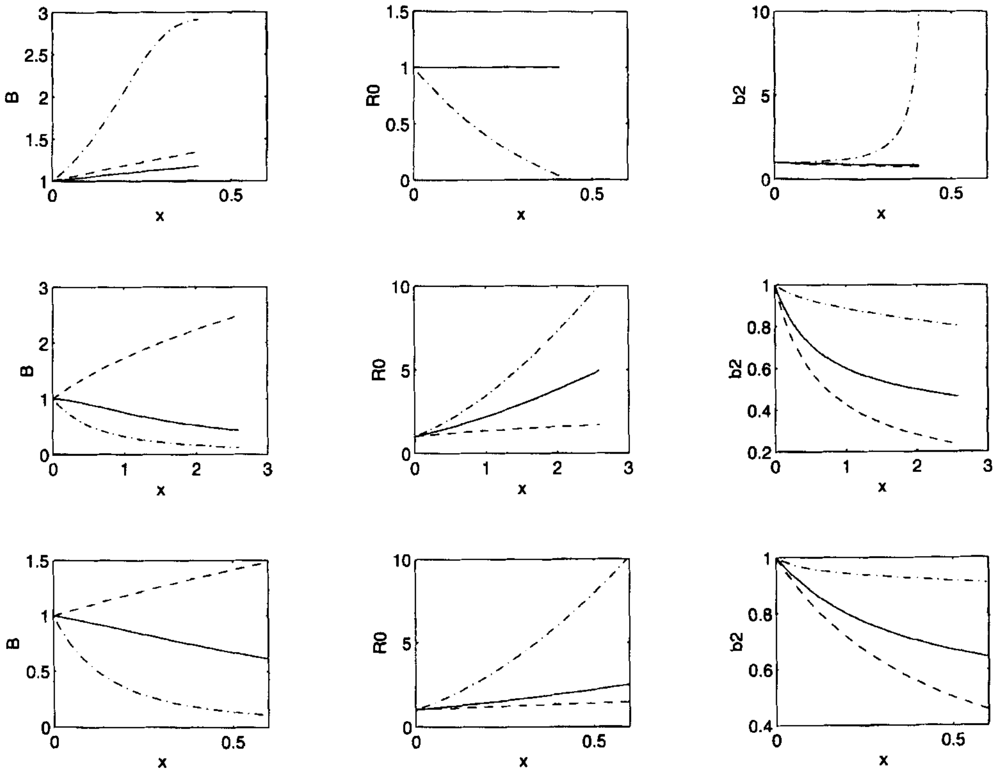

Figure 6. Leading-order axial velocity component (left column), mean radius (middle column) and thickness (right column) for inertia-dominated, downward, annular liquid jets. Top row: $dR_0(0)/dz = -0{\cdot}25$; middle row: $dR_0(0)/dz = 0$; bottom row: $dR_0(0)/dz = 0{\cdot}25$; $We = 100, Fr = 1, \bar{A} = 1$ (full lines), $\bar{A} = 0$ (broken lines), $\bar{A} = 10$ (chain lines)

forces tend to decrease the jet's thickness, while the gravitational acceleration increases the axial velocity component and decreases the jet's thickness. These two body forces are responsible for the shapes presented in the second row of Figure 6.

Figure 6 indicates that the results for outward flows at the nozzle exit exhibit the same trends as those for axial ones.

Figure 7 shows the effects of the Weber number and nozzle exit angle on the axial velocity component, mean radius and thickness of inertia-dominated, downward, annular liquid jets. The most remarkable aspects of this figure are that (i) there are very few differences between the results for $We \geqslant 100$ for zero and positive angles at the nozzle exit, (ii) annular jets with $We = 1$ merge on the symmetry axis for the nozzle exit angles considered in this paper, (iii) the jet's mean radius is a monotonically increasing function of z for $We = \infty$ and the values of the parameters considered in this paper and (iv) the non-homogeneous, conservative body forces cause a flow acceleration near the nozzle for inwardly directed flows at the nozzle exit; this acceleration is followed by a deceleration as indicated in the relative maximum of the first row of Figure 6.

In Figure 8 the effects of the Froude number and nozzle exit angle are illustrated. This figure shows that the annular liquid jet's fluid dynamics is nearly independent of the Froude number for $Fr \geqslant 1000$; the axial velocity component is very sensitive to the nozzle exit angle and decreases as z increases for

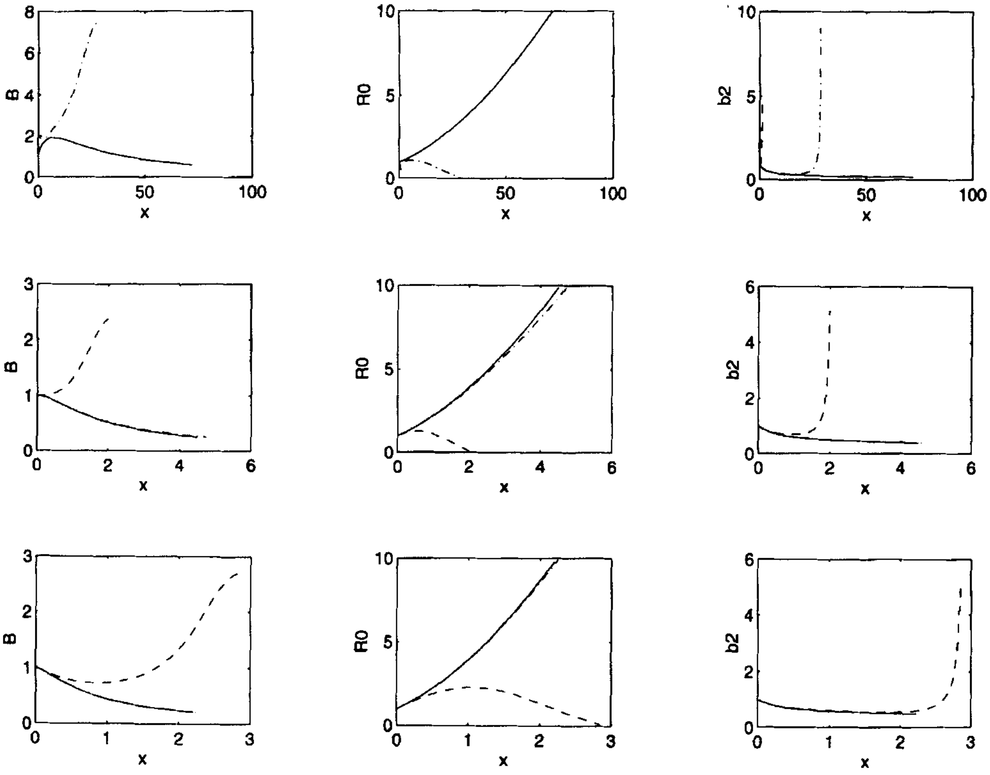

Figure 7. Leading-order axial velocity component (left column), mean radius (middle column) and thickness (right column) for inertia-dominated, downward, annular liquid jets. Top row: $dR_0(0)/dz = -0{\cdot}25$; middle row: $dR_0(0)/dz = 0$; bottom row: $dR_0(0)/dz = 0{\cdot}25$; $A = 1, Fr = 1$, $We = \infty$ (full lines), $We = 1$ (broken lines), $We = 100$ (chain lines)

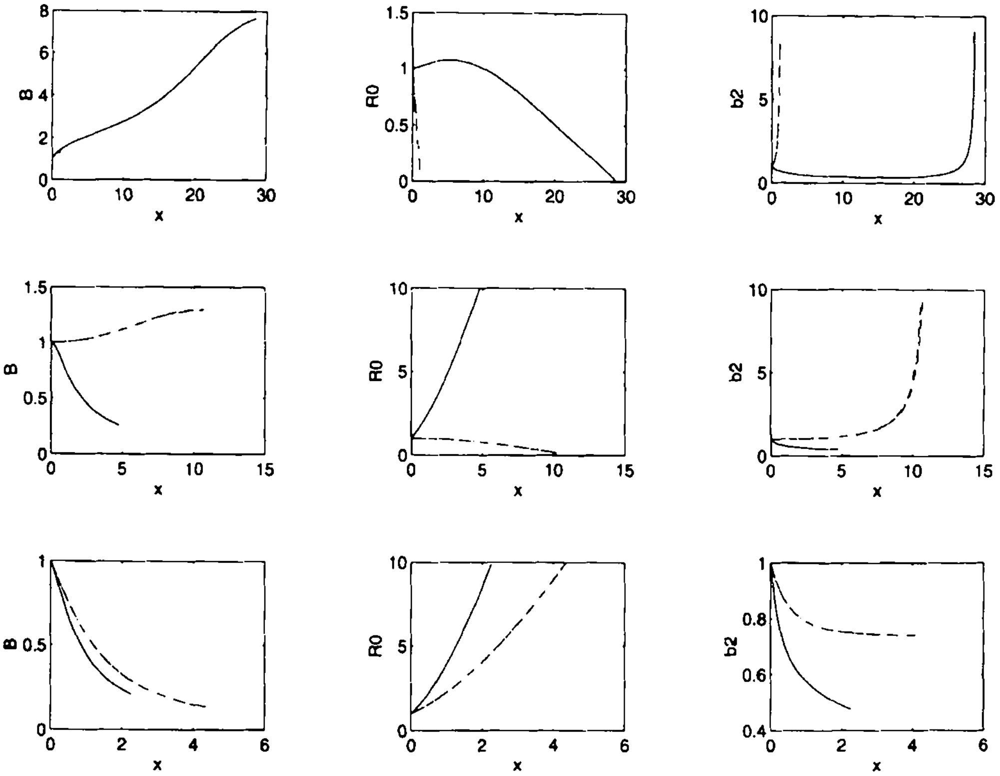

Figure 8. Leading-order axial velocity component (left column), mean radius (middle column) and thickness (right column) for inertia-dominated, downward, annular liquid jets. Top row: $dR_0(0)/dz = -0{\cdot}25$; middle row: $dR_0(0)/dz = 0$; bottom row: $dR_0(0)/dz = 0{\cdot}25$; $We = 100, A = 1, Fr = 1$ (full lines), $Fr = 1000$ (broken lines), $Fr = \infty$ (chain lines)

$Fr = 1$ and axially and outwardly directed flows at the nozzle exit, whereas it increases with z for inward flows. Figure 8 also shows that for inward flows at the nozzle exit and $Fr = 1$ the jet's mean radius first increases and then decreases as a function of z.

Figure 9 indicates that the axial velocity of capillary, downward, annular liquid jets is an increasing function of z and increases very little for $Fr \geqslant 1000$, while the axial velocity component is a monotonically decreasing function of the non-homogeneous, conservative body forces.

5. CONCLUSIONS

Perturbation methods have been employed to analyse the fluid dynamics of inviscid, irrotational, incompressible, axisymmetric, slender, thin, annular liquid jets subject to gravity, surface tension and non-homogeneous, conservative body forces when these forces are important at leading order. The small parameter is the jet's slenderness ratio, which is the ratio of the jet's mean radius at the nozzle exit to a characteristic axial dimension. Depending on the magnitude of the Weber number, two different flow regimes have been identified. The inertia-dominated regime is characterized by large Weber numbers and requires the use of the dynamic (normal stress) boundary conditions at fourth order in the perturbation parameter to close the leading-order equations. The capillary regime achieves closure at leading order, is characterized by small Weber numbers and predicts a cylindrical jet at

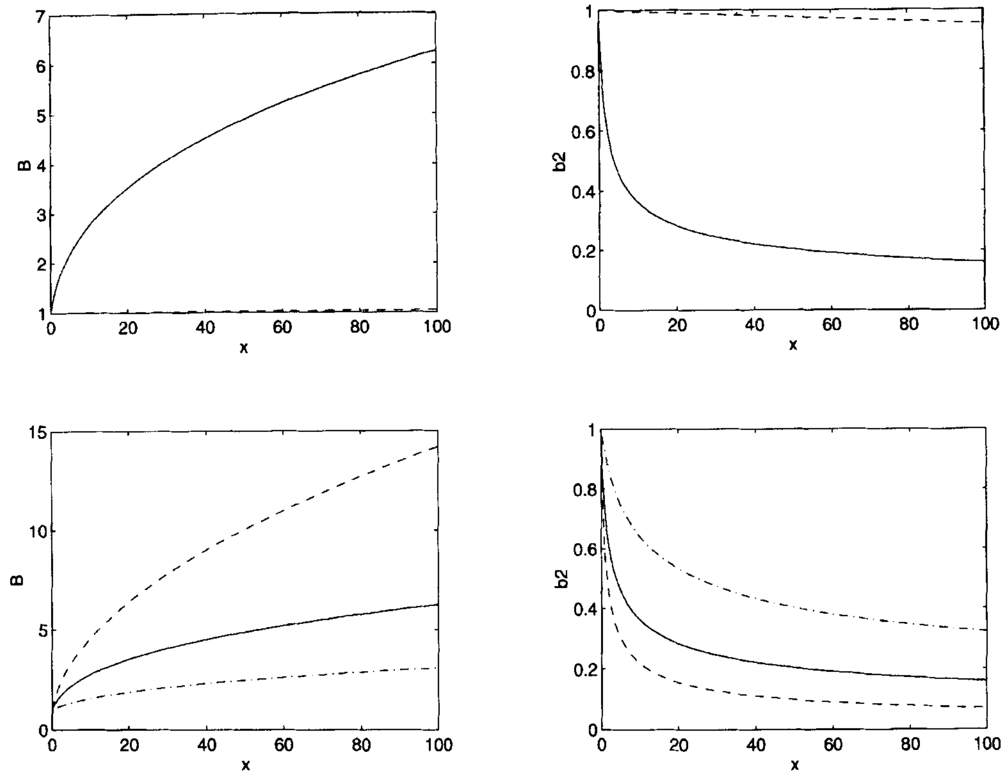

Figure 9. Leading-order axial velocity component (left column) and thickness (right column) for capillary, downward, annular liquid jets. Top row: $\bar{A} = 1, Fr = 1$ (full lines), $Fr = 1000$ (broken lines), $Fr = \infty$ (chain lines); bottom row: $Fr = 1, \bar{A} = 1$ (full lines), $\bar{A} = 0$ (broken lines), $\bar{A} = 10$ (chain lines)

leading order. It has also been shown that the capillary regime has analytical solutions for steady flows, whereas the inertia-dominated one is highly non-linear on account of the inertia terms and non-homogeneous, conservative body forces and requires a numerical solution.

Steady state solutions of the inertia-dominated regime for both upward and downward, annular liquid jets have been obtained by solving the steady equations by means of a fourth-order-accurate Runge–Kutta method for different values of the Froude and Weber numbers, body force constant and nozzle exit angle. Solutions have also been obtained by solving the time-dependent governing equations by means of an adaptive finite difference technique which maps the time-dependent, curvilinear geometry of annular liquid jets into a unit square until an asymptotic steady state is reached. The results of the two techniques were nearly identical for the flow conditions analysed in this paper.

The numerical results show that the fluid dynamics of steady, annular liquid jets is very sensitive to the Froude and Weber numbers and nozzle exit angle in the presence of non-homogeneous, conservative body forces. For upward jets with inwardly or axially directed velocities at the nozzle exit the effects of the non-homogeneous, conservative body forces is to increase the leading-order axial velocity component, decrease the jet's mean radius and move the stagnation point downstream. For downward jets with outward velocity at the nozzle exit the axial velocity component decreases monotonically as the non-homogeneous, conservative body forces are increased.

It has also been shown that the fluid dynamics of both upward and downward annular liquid jets is almost independent of the Froude and Weber numbers for sufficiently large values of these parameters.

ACKNOWLEDGEMENTS

The research reported in this paper was supported by Project PB94-1494 from the DGICYT of Spain. The author is grateful to the Centro Europeo de Paralelismo de Barcelona (CEPBA), Spain, where some of the computations presented here were performed on a CONVEX C3480 supercomputer.

REFERENCES

1. J. I. Ramos, 'Fluid dynamics of slender, thin, annular liquid jets', *Int. j. numer. methods fluids*, **21**, 735–761 (1995).
2. B. V. Derjaguin, N. V. Churaev and V. M. Muller, *Surface Forces*, Consultants Bureau, New York, 1987.
3. J. Israelachvili, *Intermolecular and Surface Forces*, 2nd edn, Academic, New York, 1992.
4. J. C. Slattery, *Interfacial Transport Phenomena*, Springer, New York, 1990.
5. D. Gallez, N. M. Costa Pinto and P. M. Bisch, 'Nonlinear dynamics and rupture of lipid bilayers', *J. Colloid Interface Sci.*, **160**, 141–148 (1993).
6. T. Erneux and S. H. Davis, 'Nonlinear rupture of free films', *Phys. Fluids A*, **5**, 1117–1122 (1993).
7. J. I. Ramos, 'Domain-adaptive finite difference methods for collapsing annular liquid jets', *Comput. Mech.*, **11**, 28–64 (1993).